Searching for Signs of a Galactic Excess of Gravitational Waves

Serena Moseley

Carleton College

Mentor: Thomas Callister

California Institute of Technology

No source of gravitational waves from the Milky Way galaxy is known to radiate within both the amplitude and frequency ranges of Advanced LIGO or Virgo. It is, however, possible that an unknown galactic source is emitting gravitational radiation at frequencies accessible to current detectors, but is too weak to be individually resolvable. If so, it would be easier to identify the source if we could recover the sky distribution of the population. We develop a method of mapping the sky distribution of unmodeled gravitational-wave bursts to determine whether there exists a galactic excess of gravitational waves in the aLIGO-Virgo frequency band. We simulate both an isotropic population and a galactically-distributed population of gravitational-wave bursts and inject these two sets into the parameter estimation code Bayeswave in order to generate posterior probability distributions on our simulated signals sky locations. We will ultimately combine these into probability distributions of source locations for each of our two populations and demonstrate that we can correctly classify our two distributions based on their recovered localizations.

I. INTRODUCTION

A. Gravitational Wave Astronomy

General relativity predicts the existence of gravitational waves, oscillations in the space-time metric that are produced by massive, accelerating objects. Since 2015, gravitational waves have been routinely detected by the Advanced LIGO [1] and Advanced Virgo [2] experiments. Compact binary coalescences (CBCs), namely binary black hole mergers and

binary neutron star mergers, have been responsible for all of the gravitational-wave signals detected so far. Signals from CBCs have peak amplitudes at frequencies within the most sensitive band of the Advanced LIGO detectors, between approximately 100 and 1000 Hz [3]. This and the fact that compact binary objects merge at a fairly high rate in the local Universe together make these events the only gravitational-wave sources observed to date.

Besides signals from CBC mergers, the LIGO and Virgo collaborations (LSC/Virgo) search for a variety of other kinds of signals, including continuous gravitational waves, a stochastic gravitational-wave background, and gravitational-wave bursts. These searches may be grouped into one of two categories: either modeled or unmodeled searches, depending on the signal morphology. In modeled searches, such as those for CBCs, we can predict deterministically what the gravitational-wave signal should look like in the data. We can create template waveforms spanning the space of possible CBC signals and search through the data for a match [4]. In contrast, other gravitational-wave signals involve so many unknowns that we cannot know beforehand what they may look like in the data. For this reason, LSC/Virgo also conduct unmodeled searches that don't rely on strong a priori assumptions about the form of the signal. Burst searches are generally unmodeled searches for signals from an unknown transient event. Examples of events that produce gravitational-wave bursts include supernovae and glitching neutron stars, in which a spinning neutron star suddenly changes its spin period [5]. For this project, we will broadly work within the realm of burst searches.

B.   Galactic Excess of Gravitational Waves

In nearly every electromagnetic frequency band, the Milky Way stands out as the brightest source in the sky. Given the recent discoveries of gravitational waves, a new "messenger" of astronomical information, we might expect the galaxy to be a similarly bright source of gravitational radiation in the sky. In fact, we already know that such a galactic excess must exist due to the vast quantity of white dwarf binaries that inhabit the Milky Way [6]. These binaries systems, either resolvable or unresolvable, are a significant source of gravitational radiation in the galaxy [5]. However, although we know galactic white dwarf binaries exist, we cannot detect them with current ground-based detectors. These systems emit gravitational radiation at frequencies that are several orders of magnitude too low to be

detected by either Advanced LIGO or Advanced Virgo. This is illustrated in Fig. 1, which graphs the frequency range of the galactic white dwarf population as well as the sensitivity curves of the current ground-based detectors. As the figure demonstrates, we can expect white dwarf binaries to be detectable by the Laser Interferometer Space Antenna (LISA).
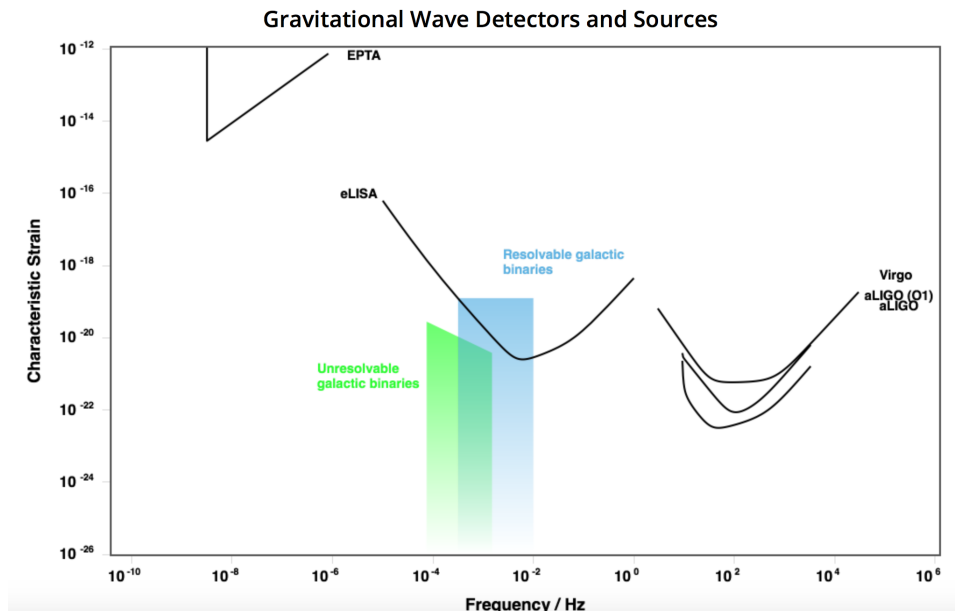

FIG. 1: A plot of the frequency band for unresolvable and resolvable galactic binaries, as well as the sensitivity of Advanced LIGO [7]. The frequency band of the galactic binaries is out of range of the Advanced LIGO sensitivity curve.

While we have yet to identify any galactic excess of gravitational waves in the detectors' output, it may be the case that an unknown galactic source is emitting radiation at frequencies accessible to Advanced LIGO and Advanced Virgo. If such sources do exist, they are likely weak as no associated signals have been clearly detected so far. Even if each burst is too weak to detect individually, we can try to detect their combined population by examining the sky distribution of burst triggers. If a real galactic population exists, we can expect the apparent sky direction of the triggers to align with the galaxy. Otherwise, an isotropic distribution in which the sky direction appears random would imply that a detectable galactic population does not exist. Separately, it is likely that the detectors will one day discover some previously unknown source population. Once this happens, we will need to be able to identify the source population; knowing the population's distribution on the sky will help to characterize it. Thus we seek to develop a method of mapping the sky distribution of unmodeled gravitational-wave bursts. We will seek to apply this method to

determine whether there exists a galactic excess of gravitational waves in the LIGO-Virgo frequency band.

II.   SIMULATED BURST INJECTIONS

We simulated gravitational-wave bursts in the form of Sine-Gaussians. Equation (1) models this Sine-Gaussian,

$$s(t) = A \left(e^{-(t-t_0)^2/\tau^2} \right) \cos \left(2\pi f_0 t + \phi_0 \right), \tag{1}$$

where A is the signals amplitude, t_0, f_0, and ϕ_0 are constants and τ is the characteristic width of the burst. τ relates to Q, the quality factor of the waveform through Eq. (2):

$$Q = 2\pi f_0 \tau. \tag{2}$$

The quality factor is approximately the number of sinusoidal cycles that the waveform completes. Our simulated bursts are all transient events with a frequency of $200 Hz$ and a relatively low quality factor of 5. Fig. 2 plots a single injection's signal.
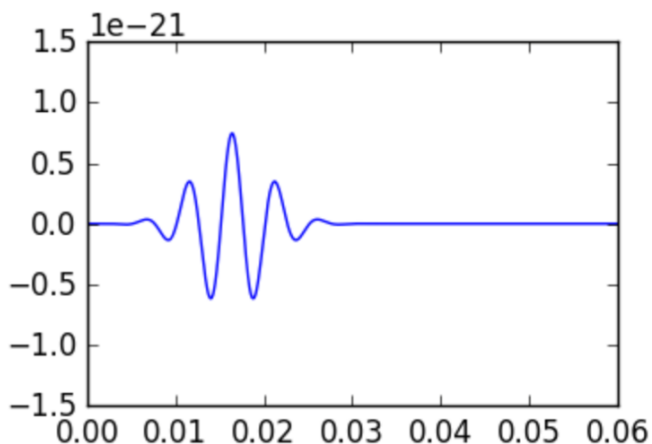

FIG. 2: The signal of one of our simulated burst events that was injected into Bayeswave. The duration in seconds is plotted along the x-axis and the strain of the signal is plotted along the y-axis.

III.   INJECTION POPULATIONS

We generate two populations of gravitational-wave bursts. The first population contains 2000 simulated burst events whose source locations were randomly generated according to an isotropic distribution. The second population also contains 2000 injections, but their positions were randomly generated according to a model of the galactic stellar distribution we developed. All of the injected signals of both populations have an SNR (signal-to-noise ratio) that ranges from about 0 to 35. In both populations, the injected signals are timed 50 seconds apart, such that the total duration of each population of bursts spans the length of a sidereal day.

A.   Isotropic Population

We generate our isotropic injections by allowing their right ascension and declination values to be uniformly distributed on the sky. Thus, there is no preferred direction for the sources of the simulated bursts.

B.   Galactic Population

Our second set of injections is meant to represent a population of gravitational-wave bursts that are originating within the Milky Way galaxy. As such, their right ascension and declination values are not determined from a uniform distribution, but rather have a preferred direction on the sky. In order to create these injections such that they have a randomly generated source position that corresponds to the position of the galaxy on the sky, we need to develop a suitable model of the distribution of stellar material in the galaxy.

1.   Modeling the Galactic Distribution

The Milky Way galaxy appears on our night sky as a long disk of stars, gas, and dust. The structure of this galactic disk can be broken down into two sub-components: a thin and thick disk comprised of two distinct stellar populations, as seen in Fig. 3. The thin disk encompasses the region of current star formation in the galaxy. It has a smaller volume yet greater density of stars than the thick disk. The thick disk, by comparison, is composed of

older stars at a density of about 8.5% the star population density inside of the thin disk [10].
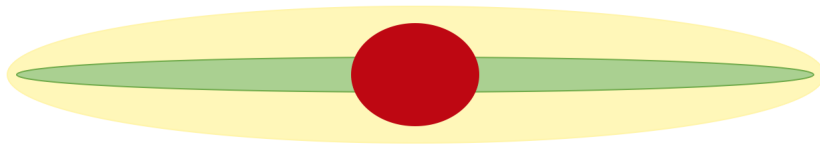

FIG. 3: A diagram of the galactic disk structure. The red circle represents the galactic bulge, while the green and yellow disks represent the thin and thick disks respectively. The scale height of the Milky Way's thin disk is about 350 pc while the scale height of the thick disk is about 1000 pc [10].

We can model the distribution of stars in the Milky Way galaxy by combining empirical knowledge about the thin and thick disks to generate the stellar number density function expressed in Eq. (3),

$$n(z,r) = n_0 \left(e^{-z/z_{\text{thin}}} + 0.085 e^{-z/z_{\text{thick}}} \right) e^{-r/h_R}, \tag{3}$$

where z is the vertical height above the mid-plane of the Galaxy, r is the radial distance from the Galactic center, n_0 is the relative density coefficient, z_{thin} is the scale height of the thin disk, z_{thick} is the scale height of the thick disk, and h_R is the disk scale length. This equation is modeled in cylindrical coordinates, however ϕ does not appear in the function because there is no preferred ϕ direction [10].

We will use Eq. (3) to simulate a population of sources distributed randomly throughout the galaxy. We will say that the probability, $p(z,r,\phi)$, of a gravitational wave occurring at the position (z,r,ϕ) is directly proportional to Eq. (3). As the probability must sum to 1 over all space, we can further say that the volume integral of $p(z,r,\phi)$ over all space must equal 1. Combining this with Eq.(4)

$$dV = r\,dr\,d\phi\,dz, \tag{4}$$

allows us to derive three normalized, independent probability density functions (PDFs) for each coordinate. Through integration, we can derive their cumulative density function (CDF) counterparts as expressed in Eq. (5), (6), (7):

$$c_z(z) = \begin{cases} 1 - z_0(z_{\text{thin}}e^{-z/z_{\text{thin}}} + 0.085z_{\text{thick}}e^{-z/z_{\text{thick}}}) & z > 0 \\ z_0(z_{\text{thin}}e^{z/z_{\text{thin}}} + 0.085z_{\text{thick}}e^{z/z_{\text{thick}}}) & z \leq 0 \end{cases}, \tag{5}$$

$$c_r(r) = 1 - \frac{r}{h_R}e^{-r/h_R} - e^{-r/h_R}, \tag{6}$$

$$c_\phi(\phi) = \frac{\phi}{2\pi}, \tag{7}$$

where z_0 is the normalization constant for the z-coordinate PDF,

We then invert these three CDFS to obtain z, r, and ϕ as a function of cumulative probability. The CDFs for z and r cannot be readily inverted, so we must generate random samples and interpolate a numerical solution for both. We can convert random c values on the interval (0,1) to random z, r, and ϕ coordinates and plot these coordinates to create a model of the galaxy (Fig. 4). We can also convert from cylindrical to Cartesian, galactic, and ultimately equatorial coordinates. The relationship between galactic (b and l) and equatorial coordinates (α and δ) is as follows in Eq. (8), (9), (10):

$$\sin(\delta) = \sin(\delta_{NGP})\sin(b) + \cos(\delta_{NGP})\cos(b)\cos(l_{NCP} - l), \tag{8}$$

$$\cos(\delta)\sin(\alpha - \alpha_{NGP}) = \cos(b)\sin(l_{NCP} - l), \tag{9}$$

$$\cos(\delta)\cos(\alpha - \alpha_{NGP}) = \cos(\delta_{NGP})\sin(b) - \sin(\delta_{NGP})\cos(b)\cos(l_{NGP} - l), \tag{10}$$

where NGP refers to the North Galactic Pole and NCP refers to the North Celestial Pole. Equatorial coordinates map directly to right ascension and declination, with α representing right ascension and δ representing declination.

We apply these equations to create a model of the distribution of stars in the Milky Way galaxy that we then use to generate random source locations for our simulated galactic bursts. Fig. 4 is a plot of 10000 of these randomly generated galactic positions.
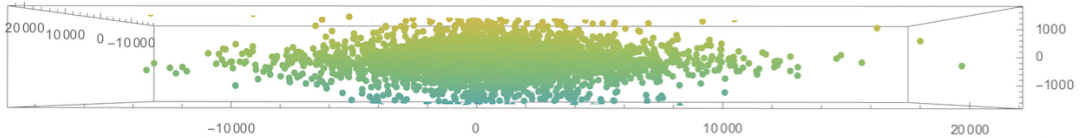

FIG. 4: A plot of 10000 sky locations for stars in the galactic disk, viewed from the galactic plane. Sky locations were randomly generated using our developed model.

We also plot these randomly drawn samples as viewed from Earth using HEALPix in Fig. 5, to demonstrate what the galaxy looks like in HEALPix visualization.
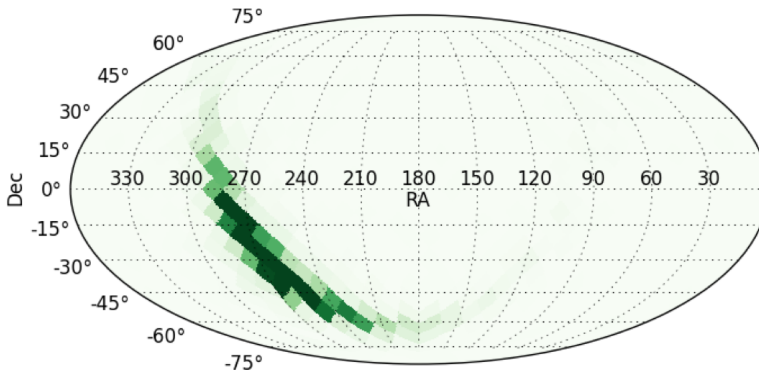

FIG. 5: A HEALPix map of our galactic samples.

IV.   MAPPING WITH BAYESWAVE

We aim to develop methods to recover the sky localizations of distinct populations such that we can tell the difference between their source locations. We simulate gravitational-wave bursts and use the parameter estimation code Bayeswave to inject and recover them. Bayeswave makes use of Bayesian statistics, particularly Bayes' Theorem, to compute posterior probabilities on the sky location of a burst.

A.   Bayesian Statistics and Bayeswave

Bayes' Theorem states that the probability of some event A given some event B, known as the posterior probability, is as follows in equation (11):

$$P(\theta \mid d) = \frac{P(d \mid \theta)\, P(\theta)}{P(d)}, \tag{11}$$

where $P(d \mid \theta)$ is the likelihood, $P(\theta)$ is the prior probability, and $P(d)$ is the evidence [9]. If we consider some parameter θ and an associated prior, we can use Bayes' Theorem to update the probability of θ given new information. Given that Bayeswave is an algorithm that reconstructs gravitational-wave signals using an arbitrary number of Sine-Gaussian wavelets [9], we can use it to produce posterior probabilities for a given parameter. We then use

these posterior samples to estimate model parameters and to reconstruct a gravitational-wave signal without a predicted waveform.

B. Bayeswave Reconstruction

We can use Bayeswave to recover parameters such as the strain of the reconstructed signal. Bayeswave can also generate posteriors on sky localization, allowing us to produce sky distributions known as skymaps.

In Fig. 6, we see a Bayeswave-reconstructed strain plot for the gravitational-wave signal from the first binary black hole merger detection, GW150914.
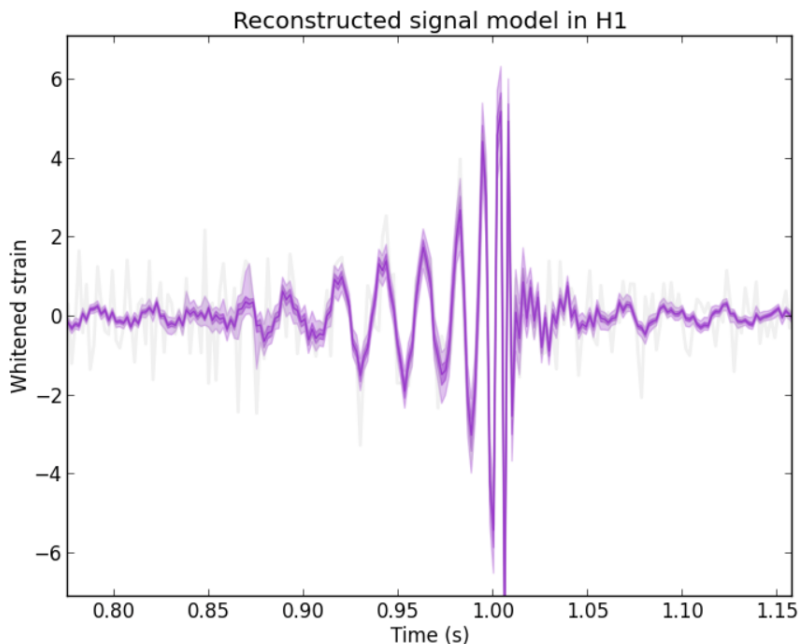
FIG. 6: A reconstructed strain plot for GW150914 generated by the megaplot.py script. The grey line is the measured strain data, the light purple line represents the posterior on the gravitational-wave strain, and the darker purple curve shows the median strain.

C. Skymaps

We can use skymaps to map the posterior probability of a signal originating from multiple locations on the sky. Skymaps are two-dimensional projections of the entire sky with colored regions to demonstrate the probability distribution of origin locations for the mapped signal.

The localization of a gravitational-wave source depends primarily on two measurements: the difference in arrival times of the signal at the two detectors, and the relative amplitudes measured by each detector. When a gravitational wave passes through the Earth and is detected by Advanced LIGO, the time difference between its arrival at the two detectors reveals information about the source location of the signal. For example, if the gravitational-wave signal arrives at both detectors at the same exact time, then the gravitational wave must have traveled along a path perpendicular to the line connecting the two detectors. This constrains the possible source directions to a single circle on the sky. In Fig. 7, we see an example of a typical gravitational wave skymap. The probability distribution of the signal's source location traces a ring on the sky.

We can partially break the remaining degeneracy by taking the orientations of the two detectors into account. The two Advanced LIGO detectors are oriented slightly differently due to the curvature of Earth's surface. These different orientations mean that the detectors are each most sensitive to slightly different regions in the sky. If a signal appears louder in one detector than it does in the other, we can say that the signal is more likely to have come from the region that particular detector is more sensitive to on the sky.
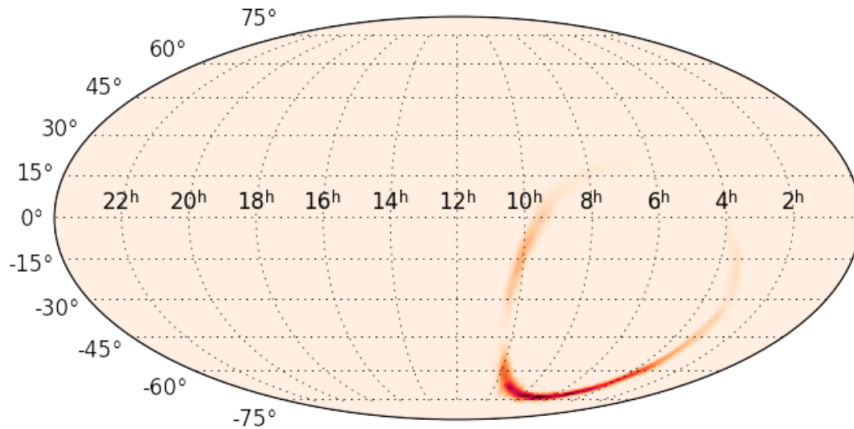

FIG. 7: A mollweide projection skymap, produced by the megasky.py script.

D. HEALPix Visualization

We can use Hierarchical, Equal Area, and isoLatitude Pix- elation (HEALPix) pixelliza-tion to visualize the skymaps of our sky localizations differently, as seen in Fig. 4 and Fig. 5. With HEALPix software, we divide our skymap up into an equal-area grid of pixels and

minimize distortion in the map projection. HEALPix allows us to store the gravitational-wave brightness for each pixel, which is the number of events coming from that pixel on the sky, as bin heights [8]. We generate these values using the posterior samples produced by Bayeswave. The default resolution for a HEALPix map is 12 pixels, but we achieve higher resolutions by increasing the number of subdivisions along each of the 12 base pixels. This parameter, known as n_{side}, determines the number of pixels in the HEALPix maps.
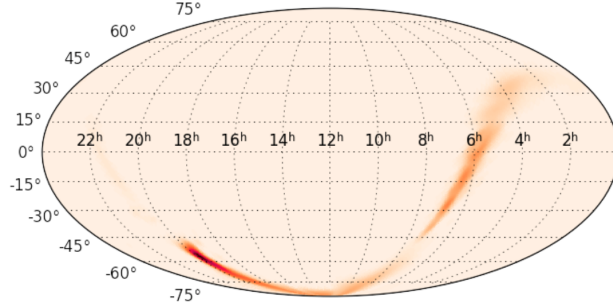
FIG. 8: The output skymap returned to us by Bayeswave for one of our individual isotropic injections.
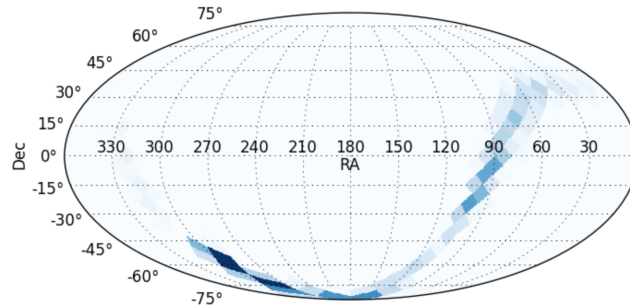
FIG. 9: This injection's corresponding HEALPix map.

V.   SAMPLE PROCESSING

For each injection, a certain number of initial samples from Bayeswave's burn-in stage are incongruent with the rest of the population and therefore need to be discarded. This can be seen in the times series for the right ascension and declination coordinates for the samples, plotted in Fig. 10 and Fig. 11. Additionally, the sample set must be downsampled to ensure each sample is independent of each other. We discard a variable number of initial samples and downsample the data set by its correlation length, computed with Acor.
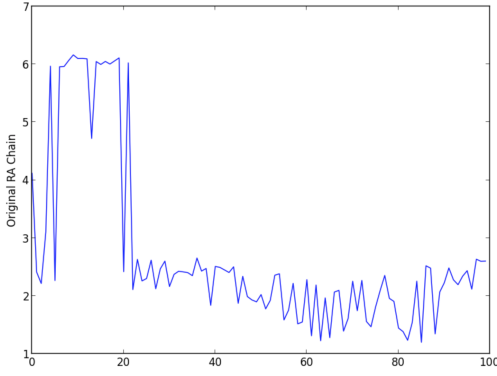
FIG. 10: A plot of the right ascension values for the first one-hundred of our 40,000 samples. Note the peak in values for the initial samples from the burn-in stage.
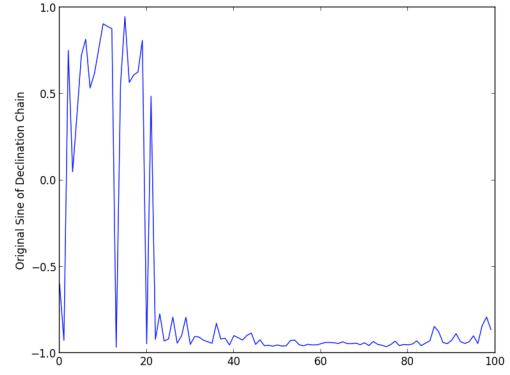

FIG. 11: A plot of the sine of the declination values for the first one-hundred of our 40,000 samples, created by our skymap.py script. Note the peak in values for the initial samples from the burn-in stage.

VI. POPULATION DISTRIBUTIONS

Given our two sets of 2000 individual injections, we are interested in examining the overall population of each set. Thus, we need a method of combining each injection's skymap into a composite probability distribution for the entire population, denoted as $\vec{c}$. We explored three methods of generating composite maps, with varying degrees of accuracy.

A. Determining Pixel with Maximum Probability

In the first method we carried out, we condense each bursts entire skymap into a single most-probable source location. We determine the pixel in each injection's HEALPix map with the most probability and assume the event did originate from that pixel on the sky. We then produce a composite map of the population by summing the bin heights of each injection's most probable pixel at its corresponding pixel on the population map. The resultant plots are shown in Fig. 12 and Fig. 13.

B. Averaging Individual Probability Distributions

Rather than discard the probabilities of the event coming from all but one pixel on the sky, we consider the entire set of pixel bin heights for each injection in our second approach. We normalize each individual injection's HEALPix map and take the bin height of each pixel
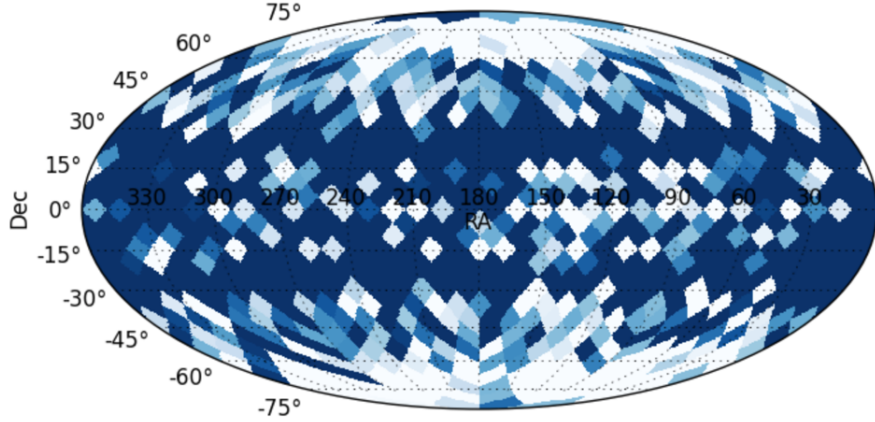
FIG. 12: The isotropic population sky distribution, produced by our maximum probability script.
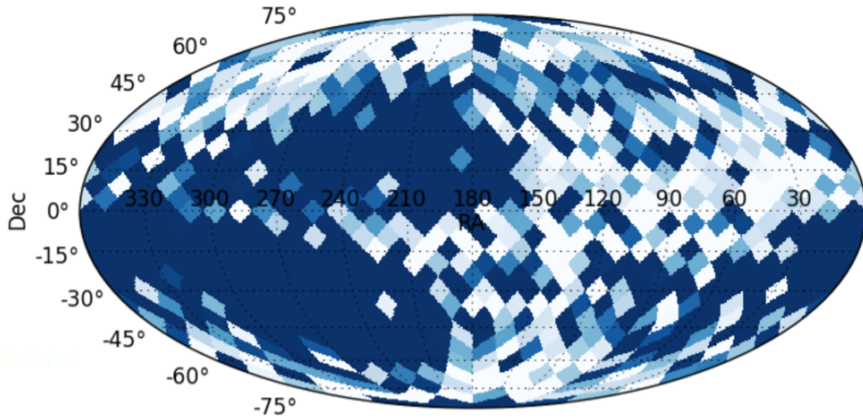

FIG. 13: The galactic population sky distribution, produced by our maximum probability script.

in the composite map to be the sum of normalized values in every injection's corresponding pixel. The resultant plots are shown in Fig. 14 and Fig. 15.

C. Multinest Approach

The final method involves Multinest, a nested sampling algorithm that conducts parameter estimation on the pixels in each HEALPix map. Multinest explores a parameter space though live points, iteratively discarding the points with the lowest likelihood so that it can ultimately converge upon the highest. We give Multinest Eq. (13) for the sampler to use in order to find the posterior probability distribution of gravitational-wave brightnesses for our populations of injected bursts.

Given the skymap data for a single burst event, d, we can write the posterior probability
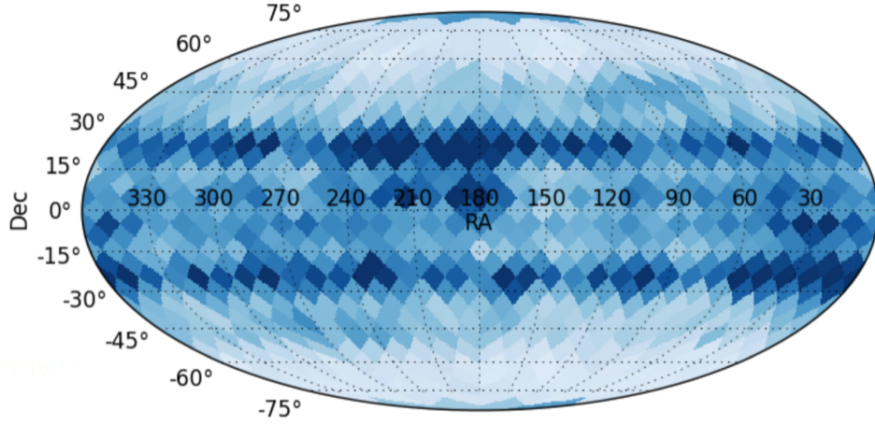
FIG. 14: The isotropic population sky distribution, produced by our average map script.
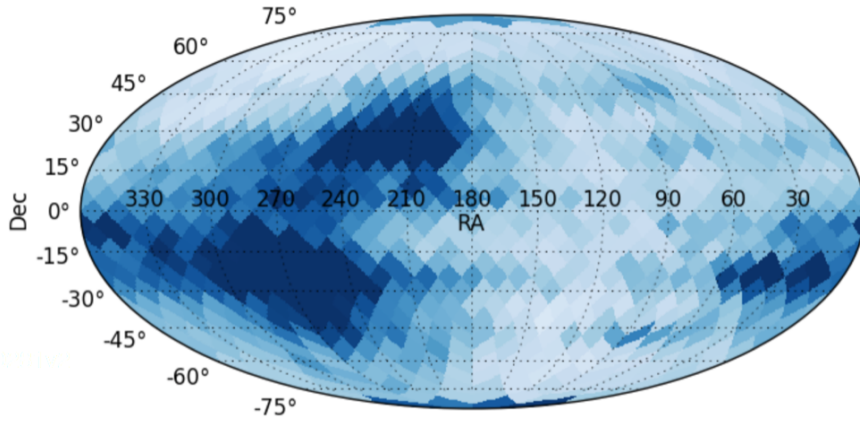

FIG. 15: The galactic population sky distribution, produced by our average map script.

of the set of gravitational wave brightnesses in each pixel for the event as Eq. (12):

$$p(\vec{c}\,|\,d) = \vec{P}\cdot\vec{c}, \tag{12}$$

where $\vec{c}$ is the vector of probabilities that a randomly-drawn gravitational-wave burst comes from each given pixel on the sky and $\vec{P}$ denotes the set of likelihoods integrated across each HEALPix pixel.

We can generalize Eq. (12) to apply to a population of events:

$$p(\vec{c}\,|\,\{d\}) \propto \prod_{d_i} \vec{P}_i\cdot\vec{c}. \tag{13}$$

Equation (13) is what Multinest ultimately uses to generate maps of the population sky localization. The resultant plots are shown in Fig. 16 and Fig. 17.
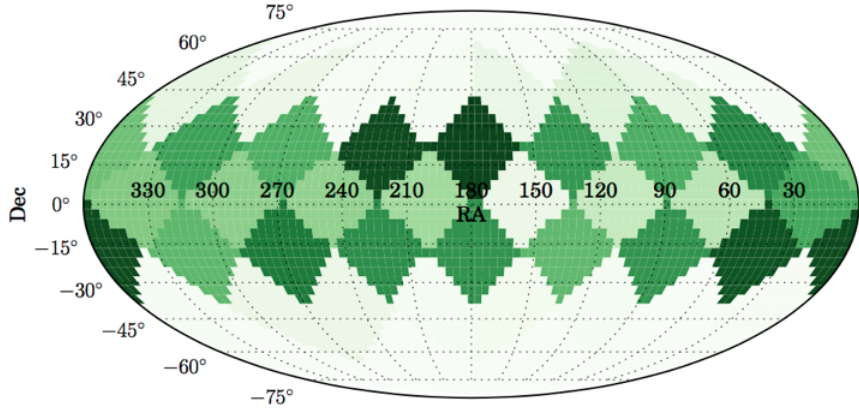
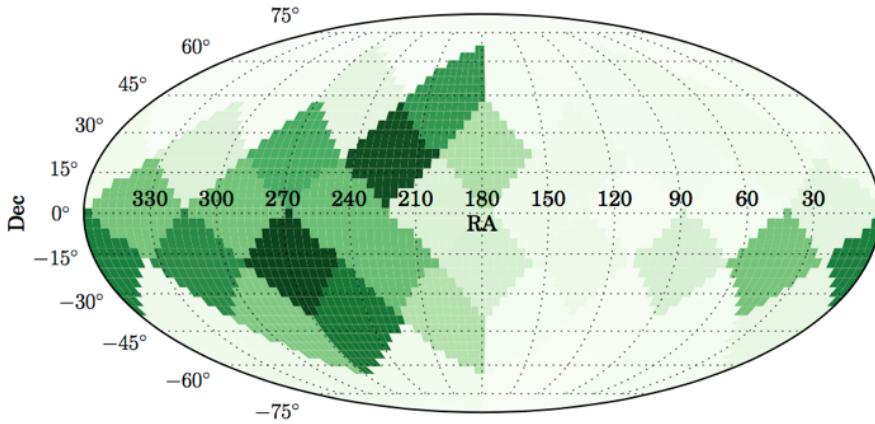FIG. 16: The isotropic population sky distribution, produced by Multinest.

FIG. 17: The galactic population sky distribution, produced by Multinest.

D. Discussion

1. Method Comparisons

In combining the individual skymaps in each injection set to produce a probability distribution of source locations for the two event populations, we see that the most detailed map is produced by our averaging method. The first method is the crudest of the three, and is used to merely check that the resultant maps of our two populations look noticeably different. Our second method of averaging the individual injections' maps produces composite maps with the most detail. In these, it is easiest to discern notable features.

Technically, the Multinest approach is the most statistically-accurate of our three methods. It is not entirely accurate to add when combining probability distributions, as we do in our first two methods as an approximation. Multinest is a computationally-intensive

program, however, and thus the produced maps are not as detailed as our averaged maps. This sampling algorithm's runtime depends on the number of dimensions in the relevant parameter space. Higher resolution HEALPix maps have a greater number of pixels, and thus, a larger number of parameters. Therefore, Multinest takes too long to converge on the most probable distribution when the resolution of the map is too large.

2. Population Features

Based on which population of gravitational-wave bursts is mapped, we expect to see specific features in the map. For the isotropic population, we expect the composite map to be featureless. The isotropic population is comprised of events uniformly distributed across the sky, so when we recover their sky distribution, we expect there to be a lack of structure within the probability distribution. For our galactic population, we expect to see the galactic disk in the composite map.

Examining our two composite probability distributions produced by our averaging method, we note that our developed method does satisfy most of our expectations. In the galactic map, we see a region of denser probability that corresponds to where the galaxy is located on the sky. This region does not appear in our recovered isotropic map, as we expected.

Our isotropic map, however, is not entirely featureless. We see some structure in the probability distribution that is azimuthally symmetric. This heavily implies that this structure is due to detector bias towards some directions on the sky, known as the antenna pattern. The effect of this bias is consistent as the Earth rotates, and thus produces structure that is horizontally smeared out across the sidereal day. We use the same reasoning to conclude that the structure we see in our galactic map cannot be due to instrumentation bias and must have been produced by the source location distribution of the events: the region of denser probability seen in the galactic map is localized to that specific region on the sky and is not azimuthally symmetric.

Overall, our resultant plots demonstrate that our method of mapping the sky distribution of a population of unmodeled gravitational-wave bursts can successfully distinguish a galactically distributed population from a non-galactically distributed set.

VII. ACKNOWLEDGEMENTS

---

[1] LIGO Scientific Collaboration, "Advanced LIGO". arXiv:1411.4547, 17 November 2014, DOI: 10.1088/0264-9381/32/7/074001.

[2] F. Acernese, et al. "Advanced Virgo: a 2nd generation interferometric gravitational wave detector". arXiv:1408.3978v3, 16 October 2014, DOI: 10.1088/0264-9381/32/2/024001.

[3] B.P. Abbott et al. (LIGO Scientific Collaboration and Virgo Collaboration), "Observation of Gravitational Waves from a Binary Black Hole Merger". Phys. Rev. Lett., Vol. 116, Iss. 6, (2016).

[4] Alexander Urban, "Signal Processing for GW Astrophysics", LIGO SURF Lecture, 25 June 2018.

[5] B.S. Sathyaprakash and Bernard F. Schutz, Physics, Astrophysics and Cosmology with Gravitational Waves, Living Rev. Relativity, 12, (2009), 2. [Online Article]: http://www.livingreviews.org/lrr-2009-2.

[6] Christopher Moore, et al. Gravitational Wave Detectors and Sources. Gravitational Wave Sensitivity Curve Plotter, Institute of Astronomy, University of Cambridge, rhcole.com/apps/GWplotter/.

[7] Andrzej Krolak, " White Dwarf binaries as gravitational wave sources " in: Einstein Online Band 04 (2010), 1001.

[8] Mark R. Calabretta and Boudewijn F. Roukema, "Mapping on the HEALPix grid". Monthly Notices of the Royal Astronomical Society, Volume 381, Issue 2, 21 October 2007, Pages 865872, https://doi.org/10.1111/j.1365-2966.2007.12297.x

[9] J.K. Kruschke, "Bayesian Data Analysis for Newcomers". Psychon Bull Rev, Psychonomic Society, 12 April 2017, DOI 10.3758/s13423-017-1272-1.

[10] Carroll, Bradley W., and Dale A. Ostlie, "An Introduction to Modern Astrophysics". Cambridge University Press, 2017.

[11] John Skilling, "Nested Sampling". AIP Conf. Proc., Volume 735, 2004, Pages 395-405. arXiv:1306.2144, AIP, DOI: 10.1063/1.1835238.

[12] Feroz, F. and Hobson, M. P. and Bridges, M., "MultiNest: An efficient and robust Bayesian inference tool for cosmology and particle physics". Mon. Not. R. Astron. Soc., Volume 398, 2009, Pages 1601-1614. arXiv:0809.3437, DOI: 10.1111/j.1365-2966.2009.14548.x.

[13] Buchner, J. and Georgakakis, A. and Nandra, K. and Hsu, L. and Rangel, C. and Brightman, M. and Merloni, A. and Salvato, M. and Donley, J. and Kocevski, D., "X-ray spectral modelling of the AGN obscuring region in the CDFS: Bayesian model selection and catalogue". Astron. Astrophys., Volume 564, 2014, Pages A125. arXiv:1402.0004, DOI: 10.1051/0004-6361/201322971.

[14] Correspondence with Tom Callister